Proceedings World Geothermal Congress 2020+1
Reykjavik, Iceland, April - October 2021

Modeling of High-Enthalpy Geothermal Projects in Fractured Reservoirs

Yang Wang[1], Stephan de Hoop[1], Denis Voskov[1,2], David Bruhn[1,3], Giovanni Bertotti[1]

[1]Delft University of Technology, Stevinweg 1, 2628 CN Delft, Netherlands

[2]Stanford University, CA 94305-4007, USA

[3]Helmholtz Center Potsdam GFZ, Germany

D.V.Voskov@tudelft.nl

Keywords: high-enthalpy geothermal, fractured reservoir

ABSTRACT

In general, high-enthalpy geothermal systems are characterized by a presence of vapor or coexistence of vapor-liquid phases. There is a complex phase transition (condensation) process during its development with cold water re-injection. Also, high-enthalpy geothermal reservoirs either contain naturally developed fractures or need induced fractures for fluid to flow at economically relevant rates. Simulation of heat production in high-enthalpy geothermal fracture systems is associated with solving complex physical process in complicated fracture networks. Besides, the existence of fracture networks magnifies the uncertainty of reservoir properties due to its wide range of scales and complex geometry, which can increase reservoir heterogeneity to a large extent.

In this work, a discrete fracture-matrix (DFM) model is used to describe the geothermal reservoir with fractures. Fractures are explicitly characterized in the model with individual grid cells. The numerical scheme is implemented within the Delft Advanced Research Terra Simulator (DARTS), which can provide fast and accurate flow response of the geothermal field. This simulation framework uses the Operator-Based Linearization (OBL) technique. In DARTS, the molar formulation is selected with pressure and enthalpy as primary variables. Besides, a fully implicit two-point flux approximation on an unstructured grid is implemented to solve the mass and energy conservation equations.

We use a realistic fracture network in this study. To achieve both accuracy and computational performance, firstly a reasonable resolution of grid discretization is determined through the comparison of solutions and convergence analysis among different sets of grid discretization. With the optimal grid resolution, we investigate the influence of geo-static and thermal parameters on thermal breakthrough and heat production. We find that the thermal production and distribution are sensitive to fracture-matrix permeability ratio, rock heat conduction and heat capacity, which can provide insights for the development of high-enthalpy geothermal reservoirs with fractures.

1. INTRODUCTION

During the development of geothermal reservoirs, the injected cold water is heated by an in-situ fluid/rock and heat can be continuously carried up to the surface by water reinjection and cycling. A high-enthalpy geothermal system is a promising resource due to the huge amount of energy it contains. For a high-enthalpy geothermal system, either single-phase (vapor) or two-phase mixture (vapor and liquid) can be present at the reservoir condition. As a typical example of a high-enthalpy geothermal system, the Geysers field (The Geysers, 2019) is the world's largest geothermal complex, producing hot steam from more than 350 wells to generate electricity in 22 power plants.

During operation of a high-enthalpy geothermal reservoir with cold water injection, both cold water vaporization and hot steam condensation can happen at the thermal front (Pruess et al., 1987). Therefore, multiphase flow and transport with complex phase changes appear in high-enthalpy geothermal systems, which introduces significant challenges for numerical simulation techniques (Coats, 1980; Wong et al., 2018; Wang and Voskov, 2019).

The development of geothermal systems can be assisted by the inherent or induced fracture networks, especially for reservoirs with a low permeable matrix. Due to the high conductivity of open fractures, the injected cold water will use the fractures as preferential flow paths. This also applies to high-enthalpy geothermal systems, which either contain lots of naturally-developed fractures and fissures or need induced fracturing to create flow paths.

To accurately simulate the fluid and heat transport in fractured geothermal systems, a proper fracture model is essential to capture the reservoir response with cold water injection. In general, there are two kinds of approaches commonly used in the representation of a fractured reservoir system. One belongs to the continuum model, of which the typical examples are the dual-porosity model proposed by Warren and Root (1963) and the dual-permeability model presented by Gerke et al. (1993a, 1993b). The continuum model is an efficient simplification of a fracture system but is not accurate enough when dealing with discontinuous fractures and large-scale fractures dominating flow (Jiang and Younis, 2015).

Another approach is the discrete fracture models, where the fracture networks are explicitly characterized by individual control volumes. Karimi-Fard et al. (2004) proposed the discrete fracture-matrix (DFM) model, which is suitable for general-purpose reservoir simulators. DFM could capture the pressure response generated by fractures accurately. However, it is computationally more expensive due to the introduction of additional degrees of freedom in the computational domain. Another approach proposed by Lee et al. (2000) includes an effective representation of fractures in a computational domain, which helps to control the number of additional degrees of freedom. However, the embedded DFM is not as accurate as the DFM in some practical situations (Li and Voskov, 2018).

In geothermal simulations, the mass and energy formulations are often tightly coupled because of the fluid thermodynamic properties (Coats et al., 1974). The fully coupled fully-implicit approach is generally adopted to solve the system of equations. During a numerical simulation, the governing equations need to be discretized in both space and time to get approximate solutions. Usually, the formulation in discretized form is nonlinear and should be linearized to facilitate solving iteratively. A Newton-based process is generally adopted to linearize the discretized formulation which requires the values of fluid properties and their derivatives.

When complex physics (i.e., multiphase compositional flow with complex chemical reactions) are present in the model, multiphase flash calculation is often necessary for accurate fluid/rock properties evaluation during each Newton iteration for molar formulation (Collins et al., 1997, Voskov and Tchelepi, 2012). Therefore, the linearization of nonlinear equations can take up a large portion of overall simulation time. Voskov (2017) proposed the operator-based linearization (OBL) approach to simplify this process and accelerate the linearization process. Like discretization in space and time, the main idea of OBL is to discretize the physics within the space of nonlinear unknowns. The OBL approach has been implemented in the newly proposed Delft Advanced Research Terra Simulator (DARTS, 2019). The DARTS framework proves its applicability for various geo-energy applications including geothermal reservoir modeling (Khait and Voskov, 2019; Wang et al., 2019).

In this study, we present the first attempt for simulation of fluid and heat transport of high-enthalpy geothermal systems at vaporized conditions in a realistic fractured reservoir. In this work, a DFM model is used to characterize the fractured geothermal reservoir. All simulations are run on DARTS with the OBL approach to linearize the physics. In the following description, we first introduce the adopted nonlinear formulation and the basics of the OBL approach. Then, the fracture model based on the practical outcrop observations is shown and the optimal grid resolution is selected according to the numerical convergence analysis. Next, the sensitivity analysis for sets of parameters is conducted and a detailed comparison for different scenarios is performed.

2. MATHEMATICAL MODEL

In this section, we briefly introduce governing equations, details of spatial and temporal discretization and linearization procedures. Further details of geothermal implementation can be found in DARTS (2019).

2.1 Governing Equations

Here, we consider the governing equations and nonlinear formulation for two-phase thermal simulation with aqueous brine. This problem can be described by mass and energy equations:

$$\frac{\partial}{\partial t}\left(\phi \sum_{j=1}^{n_p} \rho_j s_j\right) - div \sum_{j=1}^{n_p} \rho_j u_j + \sum_{j=1}^{n_p} \rho_j \tilde{q_j} = 0, \tag{1}$$

$$\frac{\partial}{\partial t}(\phi \sum_{j=1}^{n_p} \rho_j s_j U_j + (1-\phi) U_r) - div \sum_{j=1}^{n_p} h_j \rho_j u_j + div(\kappa \nabla T) + \sum_{j=1}^{n_p} h_j \rho_j \tilde{q_j} = 0, \tag{2}$$

where: ϕ is porosity, s_j is phase saturation, ρ_j is phase molar density, U_j is phase internal energy, U_r is rock internal energy, h_j is phase enthalpy, κ is thermal conduction.

The saturation constraint requires:

$$\sum_{j=1}^{n_p} s_j = 1. \tag{3}$$

In addition, Darcy's law is used to describe the fluid flow in the reservoir,

$$u_j = K \frac{k_{rj}}{\mu_j}(\nabla p_j - \gamma_j \nabla D), \tag{4}$$

where: K is permeability tensor, k_{rj} is relative permeability, μ_j is phase viscosity, p_j is pressure in phase j, γ_j is gravity vector, D is depth.

Next, Darcy's law is substituted into the governing equation to replace the velocity term and the resulting nonlinear equations are discretized with the finite-volume method in space on a general unstructured mesh and with backward Euler approximation in time:

$$V\left[(\phi \sum_{j=1}^{n_p} \rho_j s_j)^{n+1} - (\phi \sum_{j=1}^{n_p} \rho_j s_j)^{n}\right] - \Delta t \sum_{l}\left(\sum_{j=1}^{n_p} \rho_j^l \Gamma_j^l \Delta \psi^l\right) + \Delta t \sum_{j=1}^{n_p} \rho_j q_j = 0, \tag{5}$$

$$\begin{split} V\left[\left(\phi \sum_{j=1}^{n_p} \rho_j s_j U_j + (1-\phi) U_r\right)^{n+1} - \left(\phi \sum_{j=1}^{n_p} \rho_j s_j U_j + (1-\phi) U_r\right)^{n}\right] - \Delta t \sum_{l}\left(\sum_{j=1}^{n_p} h_j^l \rho_j^l \Gamma_j^l \Delta \psi^l + \Gamma_c^l \Delta T^l\right) \\ + \Delta t \sum_{j=1}^{n_p} h_j \rho_j q_j = 0, \end{split} \tag{6}$$

2.2 Transmissibility Evaluation in DFM

The capability of discretizing complex and realistic fractured reservoirs in DARTS has been extended by including the Discrete Fracture Matrix (DFM) model (Karimi-Fard et al., 2004). This model represents the fracture geometry explicitly as a lower dimensional feature, i.e. a 3D model contains 2D fractures (planes) while a 2D model contains 1D fractures (lines). This is depicted in Figure 1(b). In the DFM model, transmissibility between neighboring grid blocks is expressed as:

$$T_{12} = \frac{\alpha_1 \alpha_2}{\alpha_1 + \alpha_2}, \quad \alpha_i = \frac{A_i k_i}{D_i} \boldsymbol{n}_i \cdot \boldsymbol{f}_i, \tag{7}$$

where A_i is the contact area between two neighboring blocks, k_i is the permeability of grid block i, D_i is the distance between the centroid of the interface and the centroid of the grid block i, $\boldsymbol{n}_i$ is the unit normal to the interface inside block i, $\boldsymbol{f}_i$ is the unit vector along the direction of the line joining the grid block i to the centroid of the interface.

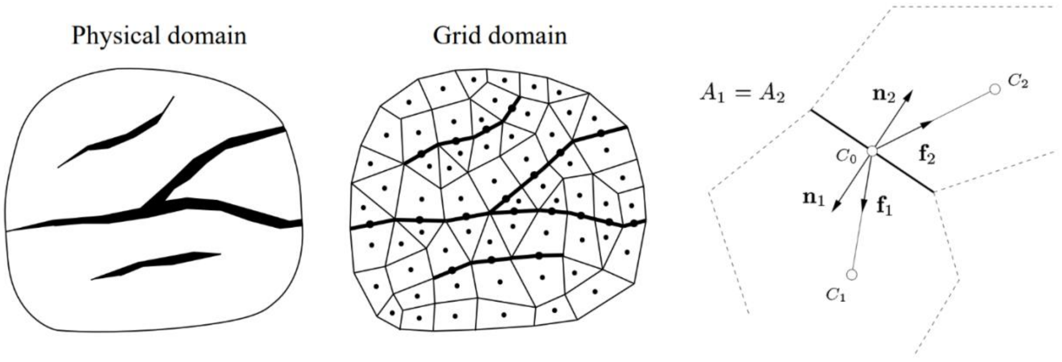

(a) **(b)** **(c)**

Figure 1: Schematic representation of the DFM model (after Karimi-Fard et al., 2004).

Fracture networks generated from outcrops usually contain complex fracture intersections that result in difficult meshing circumstances. The generated mesh, therefore, often contains artifacts that negatively impact the performance of the reservoir simulation, i.e. convergence problems and numerical inaccuracies due to non-uniformity of the control-volumes. This is solved by using a pre-processing step in which we sequentially discretize each fracture, using the desired discretization scale (predefined size of the segment).

For fracture pre-processing, we adapted a procedure suggested by Karimi-Fard and Durlofsky (2016). During the sequential procedure, we check at every iteration if the newly placed discretized fracture segment conflicts with any previously added segment. A conflict is defined here as two fracture nodes (end-points of each discretized fracture segment) that fall within a certain radius (half the discretization accuracy) of each other. This pre-processing step is computationally insignificant with respect to the main fluid-flow simulation time while still greatly improving the simulation results (accuracy and computational time). This method also allows for a fast and reliable way of creating the discretized fracture network at any desired resolution while maintaining the main characteristics of the original fracture characterization.

2.3 Operator-Based Linearization (OBL)

Based on the OBL approach, the mass and energy governing equations are distinguished into operators, which are expressed as functions of a physical state ω (Voskov, 2017; Khait and Voskov 2018). Pressure and enthalpy are taken as the unified state variables for a given control volume. Flux-related fluid properties are defined by the physical state of the upstream block, determined at interface l. The state-dependent operator is defined as a function of the physical state only.

The discretized mass conservation equation in operator form reads as:

$$\phi_0 V\big(\alpha(\omega) - \alpha(\omega_n)\big) + \sum_l \Delta t \Gamma^l (p^b - p^a) \beta(\omega) + \theta(\xi, \omega, u) = 0; \tag{8}$$

where,

$$\alpha(\omega) = \left(1 + c_r(p - p_{\text{ref}})\right) \sum_{j=1}^{n_p} \rho_j s_j ; \qquad \beta(\omega) = \sum_{j=1}^{n_p} \rho_j^l \frac{k_{rj}^l}{\mu_j^l}. \tag{9}$$

The discretized energy conservation equation in operator form is as follows:

$$\begin{aligned} \phi_0 V \left(\alpha_{ef}(\omega) - \alpha_{ef}(\omega_n)\right) + (1 - \phi_0) V U_r \big(\alpha_{er}(\omega) - \alpha_{er}(\omega_n)\big) + \sum_l \Delta t \Gamma^l (p^b - p^a) \beta_e(\omega) \\ + \Delta t \sum_l \Gamma^l (T^b - T^a) \big[\phi_0 \varepsilon_{ef}(\omega) + (1 - \phi_0) \kappa_r \varepsilon_{er}(\omega)\big] + \theta_e(\xi, \omega, u) = 0; \end{aligned} \tag{10}$$

where,

$$\alpha_{ef}(\omega) = \big(1 + c_r(p - p_{\text{ref}})\big) \sum_{j=1}^{n_p} \rho_j s_j U_j ; \quad \alpha_{er}(\omega) = \frac{1}{\big(1 + c_r(p - p_{\text{ref}})\big)}; \quad \beta_e(\omega) = \sum_{j=1}^{n_p} h_j^l \rho_j^l \frac{k_{rj}^l}{\mu_j^l}; \tag{11}$$

$$\varepsilon_{ef}(\omega) = (1 + c_r(p - p_{\text{ref}})) \sum_{j=1}^{n_p} s_j \kappa_j \ ; \qquad \varepsilon_{er}(\omega) = \frac{1}{(1 + c_r(p - p_{\text{ref}}))}. \tag{12}$$

This representation significantly simplifies the general-purpose simulation framework. Instead of performing a complex evaluation of each property and its derivatives during the simulation, we can parameterize the state-dependent operators in the space of unknowns with a limited number of supporting points and use multilinear interpolation to evaluate them (Voskov, 2017). This not only makes the linearization process simpler but also improves the performance since all expensive property evaluations can be skipped. Besides, due to the piece-wise multilinear approximation of physical operators, the system will become more linear and the performance of the nonlinear solver can be improved (Khait and Voskov, 2018).

3. FRACTURE MODEL

In this section, we describe parameters of our fractured network, explain the construction of the DFM model based on a predefined resolution scale and show the results of the numerical convergence study.

3.1 Background

The fracture network used in this work is taken from an outcrop of the Whitby Mudstone Formation (Boersma et al., 2015). The geometry of the fracture network is depicted in Figure 3, while the model size is $900\text{m} \times 1400\text{m} \times 1\text{m}$.

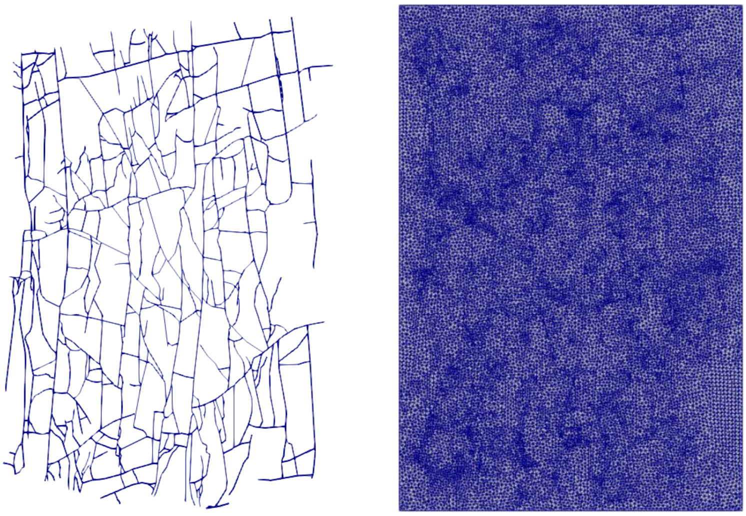

(a) (b)

Figure 3: Fracture geometry and finest grid discretization.

3.2 Results Convergence Analysis

The reasonable grid resolution is important for both accurately presenting the fracture network in the reservoir based on geological data and keeping the low computational cost. To choose a proper resolution for simulation of flow and thermal transport in fractured networks, a convergence study should be performed. In our work, four sets of discretized models, from coarsest to finest as shown in Table 1, are selected to observe the sensitivity of grid resolution to temperature profile and corresponding fluid rate at the production well. The solution from the finest resolution (Case 4) is taken as the reference and is compared with solutions generated by models with lower resolution (Case 1-3). Two different initial conditions are selected, one with vapor and liquid coexistence, while the other with single liquid water, as shown in Table 2. Test 1 corresponds with typical steam production from a hot-spot area (i.e., The Geysers, 2019), while Test 2 corresponds to deep geothermal systems containing single-phase liquid with a temperature around 600K.

Table 1: Number of discretized fracture and matrix grids under different resolutions

Case	Fracture Control Volumes	Matrix Control Volumes	Resolution
1	1388	3712	Coarse
2	2215	8710	Moderate
3	2269	11480	Fine
4	4318	37372	Finest

Table 2: Initial and development condition of two different tests

	Test 1	Test 2
Initial pressure, bar	100	350
Initial enthalpy, kJ/kg	1500	1500
Initial steam saturation	0.47	0
Injection well condition, m^3/day	400	200
Production well condition, bar	70	330

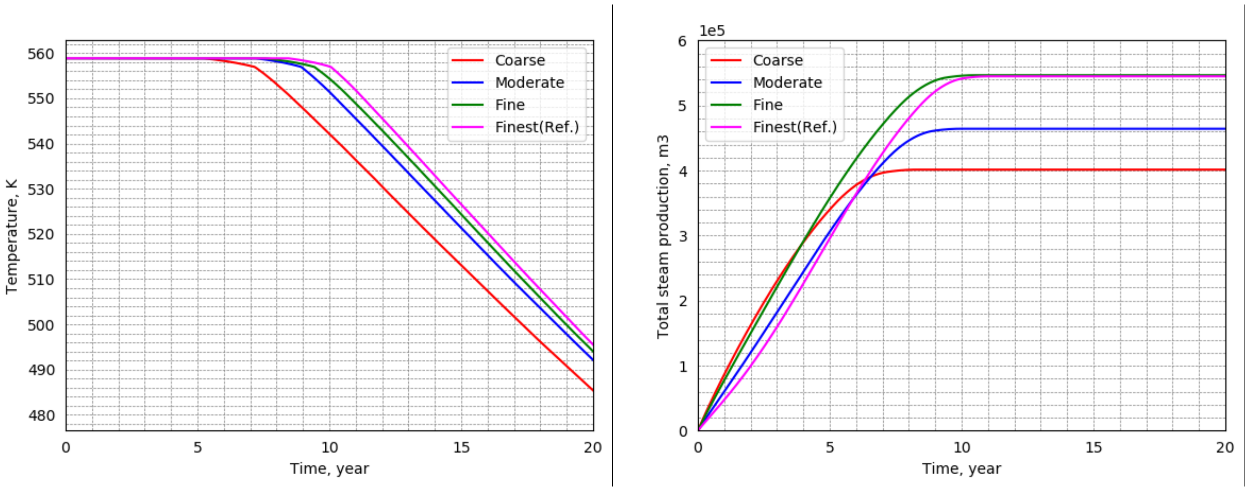

(a) **(b)**

Figure 4: Temperature and total steam production profile of the production well for Test 1 under different grid resolutions.

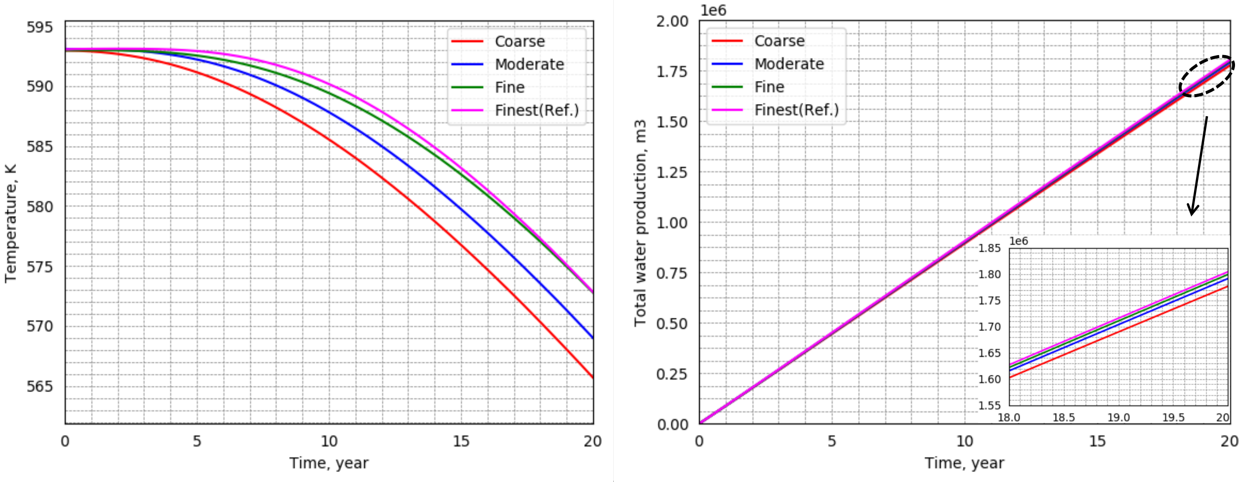

(a) **(b)**

Figure 5: Temperature and total water production profile of the production well for Test 2 under different grid resolutions.

We notice, from both Figure 4(a) and Figure 5(a) that the temperature profile of coarse resolution deviates from the reference solution significantly. This demonstrates that the coarse grid approximation introduces an inacceptable error to the thermal response. In addition, for Test 1, the production rate deviates for a coarser resolution due to nonlinearities related to the condensing steam. With the increase in grid resolution (Case 2: Moderate), the solution starts converging to the reference solution, which is also reflected in the total production curve in Figure 4(b) and Figure 5(b). For the fine model (Case 3), it converges to the reference solution in both temperature and production profile.

Figure 6 and 7 show the temperature distribution of Test 1 and 2 for different grid resolutions respectively. With refinement of the grid, the temperature distribution is more precisely depicted. As the injection rate of these two tests are different, the temperature distribution in the matrix also varies. With a lower injection rate (in Figure 7), wider low temperature distribution is observed near the injection well, which represents better heat sweep efficiency in the formation.

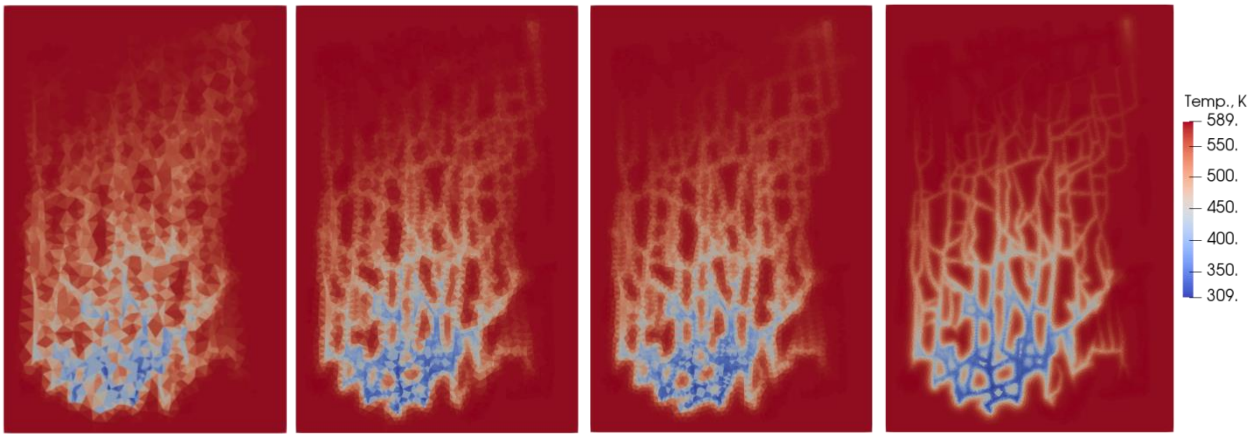

(a) (b) (c) (d)

Figure 6: Temperature distribution for Test 1 with different grid resolutions (a) coarse (b) moderate (c) fine (d) finest.

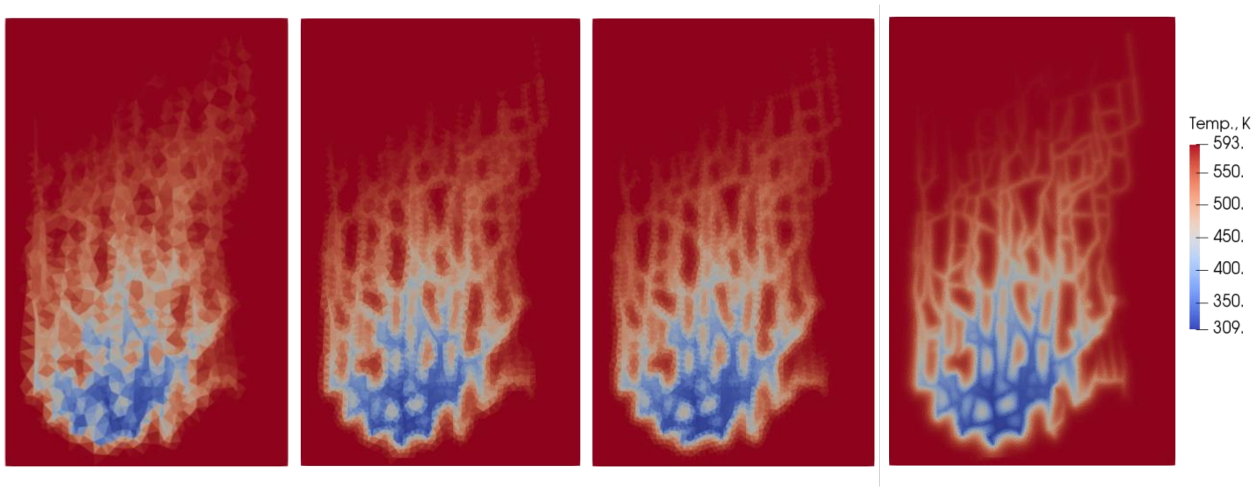

(a) (b) (c) (d)

Figure 7: Temperature distribution for Test 2 with different grid resolutions (a) coarse (b) moderate (c) fine (d) finest.

To explain why the results deviate so significantly in Test 1, we plot additional maps of pressure and saturation distribution for different grid resolutions in Figures 8 and 9 respectively. At a lower resolution, both distributions are moving forward slower due to the complex interplay between thermal transport and steam condensation. With the refinement, the pressure and saturation distributions become closer with the referenced finest model and both temperature and rate profiles at the production well matching each other.

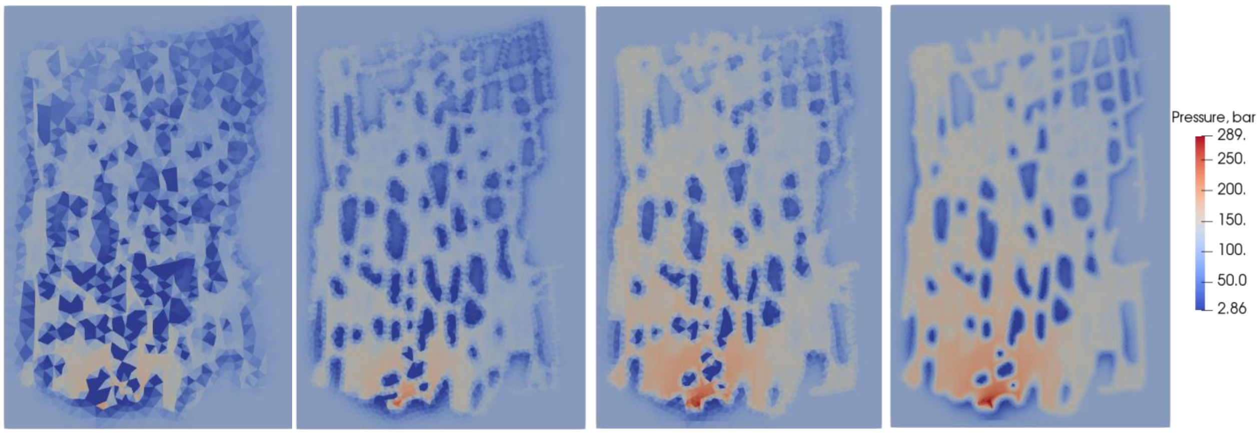

(a) (b) (c) (d)

Figure 8: Pressure distribution for Test 1 with different grid resolutions (a) coarse (b) moderate (c) fine (d) finest.

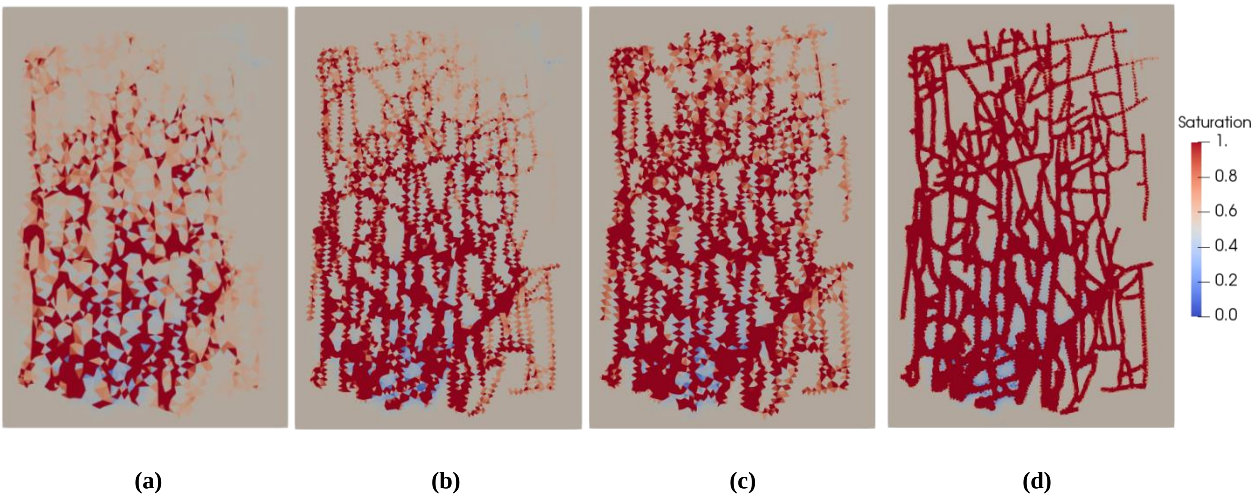

Figure 9: Saturation distribution for Test 1 with different grid resolutions (a) coarse (b) moderate (c) fine (d) finest.

The CPU time (in Figure 10) shows how the simulation time of both tests increases with the gird resolution. For Test 2, simulation time grows almost linearly in proportion to the number of control volumes in the study. However, in Test 1, the time is growing exponentially due to increased nonlinearity of a condensation process at a higher resolution. The fine resolution (Case 3) accurately predicts the dynamics of both systems and still performs at a reasonable CPU time. Therefore, we choose to use this resolution for the following sensitivity study.

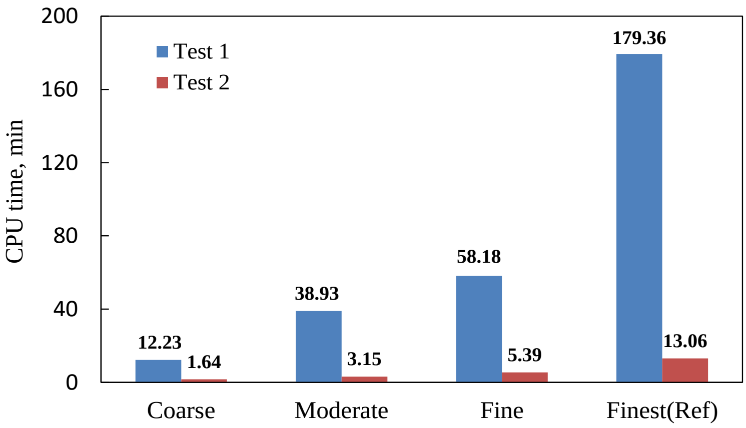

Figure 10: CPU time comparison of different grid discretizations

4. NUMERICAL RESULTS AND ANALYSIS

There are a lot of uncertainties in the subsurface formations that can impact both the heat production and lifetime of a geothermal project. Here, we investigate the influence of geo-static (k_f/k_m) and thermodynamic parameters (rock heat conductivity and heat capacity) to thermal breakthrough time in the most nonlinear case with steam condensation (Test 1). The results can provide insights for the development of high-enthalpy geothermal reservoirs with uncertainties. The base case parameter settings are listed in Table 3. Here, the parameters are selected based on the rock properties of basalts.

Table 3: Base case parameter settings

Matrix permeability, mD	1×10^{-3}	Initial pressure, bar	100
Fracture aperture, m	3×10^{-4}	Initial enthalpy, kJ/kg	1500
Fracture permeability, mD	7.5×10^{6}	Initial steam saturation	0.47
Rock heat conduction, kJ/m/day/K	180	Injection well condition, m^3/day	400
Rock heat capacity, kJ/m^3/K	2200	Production well condition, bar	70

4.1 Fracture-matrix Permeability Contrast k_f/k_m

The permeability contrast reflects the relative conductivity of fracture and matrix to fluid and heat. Depending on the geological formation, the matrix permeability can vary from very high values (porous sandstone) to almost impermeable (basalts). The permeability contrast is one of the factors with the strongest influence on heat transport and cold front propagation. It is therefore important and meaningful to analyze the development of the temperature distribution under different permeability ratios.

In this study, the cubic law (Berkowitz, 2002) is taken to describe the flow transmissibility in the fractures. The fracture permeability is expressed as:

$$k_f = \frac{b^2}{12} \tag{13}$$

Here, a set of fracture-matrix permeability ratios are chosen and examined to observe the thermal response with different cases. As shown in Table 4, the fracture aperture is fixed so that the fracture permeability is constant. Variation in permeability contrast is achieved by adjusting the matrix permeability from high to low in 3 cases. Here we choose matrix permeability typical for different types of rocks: sandstone, carbonates and basalts.

Table 4: Fracture-matrix permeability ratio

Case	Matrix perm. $\mathrm{k_m}$ (mD)	Fracture aperture (m)	Fracture perm. $\mathrm{k_f}$ (mD)	$\mathrm{k_f/k_m}$
1	10^2	3×10^{-4}	7.5×10^6	7.5×10^4
2	10^0			7.5×10^6
3	10^{-3}			7.5×10^9

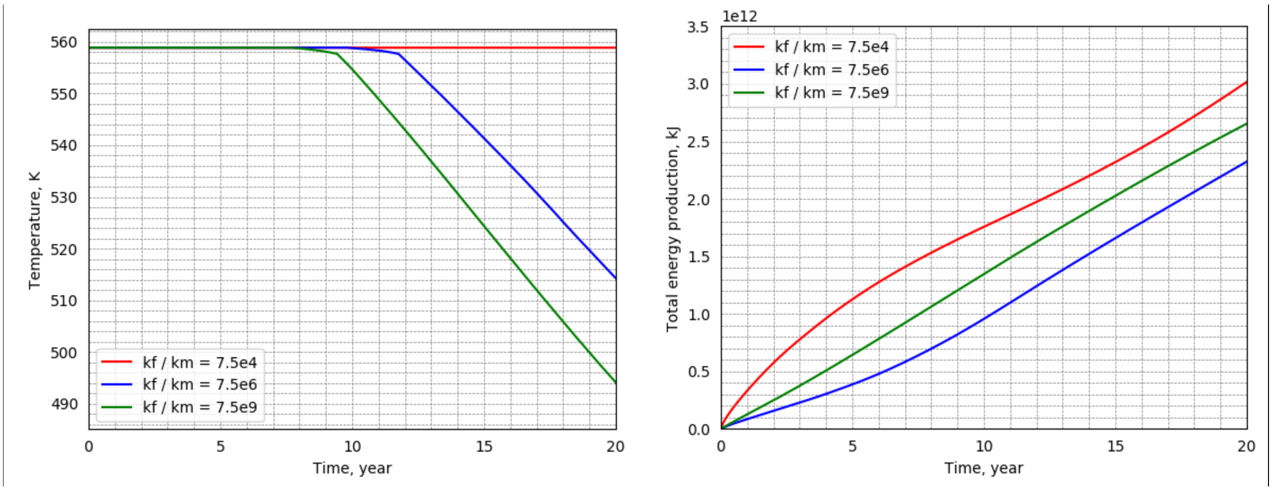

(a) (b)

Figure 11: Temperature and total energy production of production well with different fracture-matrix permeability contrast.

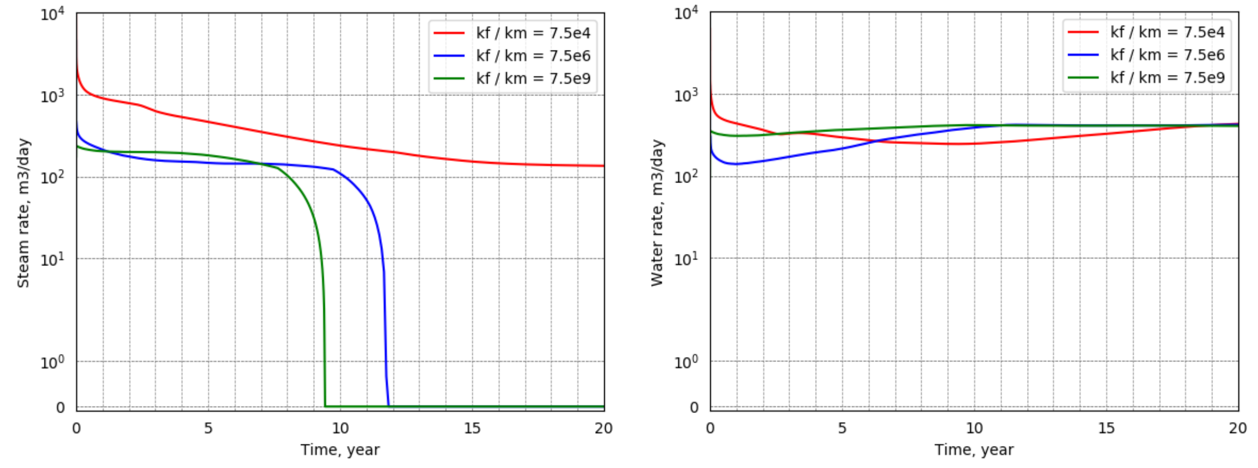

(a) (b)

Figure 12: Steam and water rate of production well with different fracture-matrix permeability contrast.

Figure 11 illustrates the impact of fracture-matrix permeability contrast to the temperature profile at the production well. With large contrast, the thermal breakthrough happens much faster than for the one with small contrast, since, in this scenario, the fracture will dominate the flow and almost no flow happens in the matrix. This effect is more obvious in Figure 13. Due to the high conductivity of the fracture network, it creates the high-flow channels which will accelerate the fluid transport towards the production well. Correspondingly, the heat will be carried by convective flow in the fracture and move forward quickly. However, more uniform thermal displacement is observed in the case with low fracture-matrix permeability contrast. As shown in Figure 13(a), the thermal front propagates much slower, and a larger part of the matrix is swept during the displacement.

Figure 12 displays the steam and water production rate with different permeability contrasts. There is a variation in the rate profile for different permeability contrasts. Through the steam rate curve, we can identify when the cold-water displacement front reaches the production well. For a large permeability contrast, the saturation front reaches the production well much earlier than the one with low permeability contrast. It should be noted that the pressure distribution in different cases varies, which explains the differences in rate profiles under different permeability contrast.

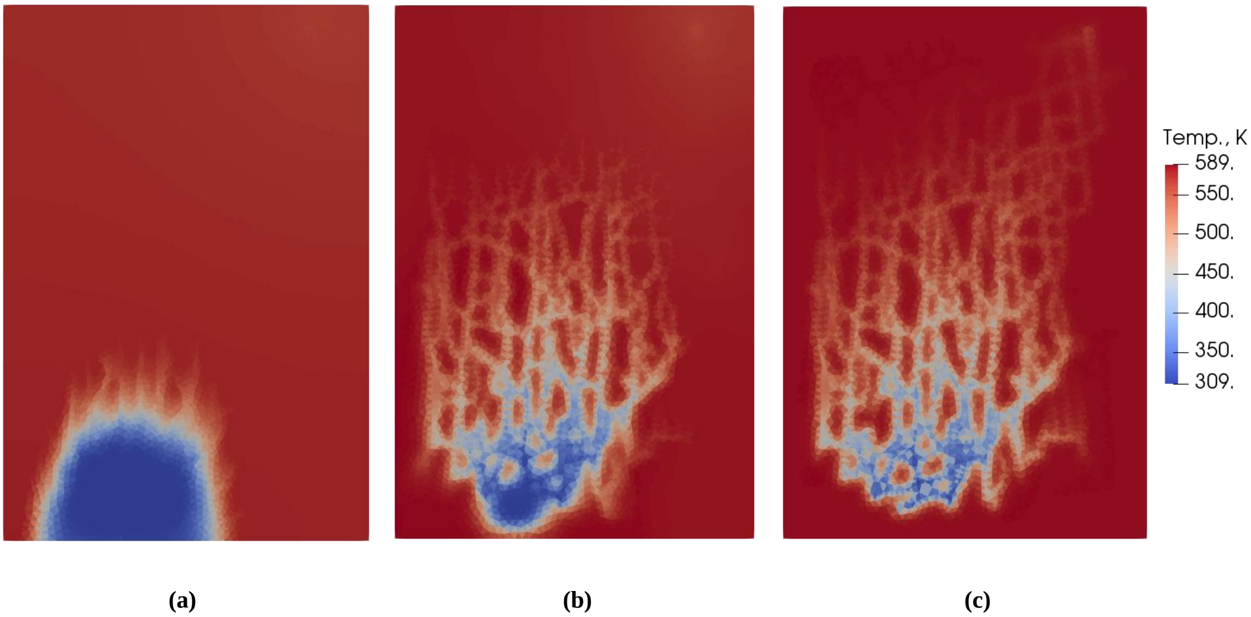

(a) **(b)** **(c)**

Figure 13: Temperature distribution for different fracture-matrix permeability ratio (a)7.5×10^{4}(b)7.5×10^{6}(c)7.5×10^{9}.

4.2 Rock Heat Conduction

Conductive heat flow is associated with the temperature gradient in both fluid and rock. According to Shetty et al. (2018), heat conduction can play an important role in the thermal breakthrough time since it can delay the thermal propagation through heating up the cold front. In a fractured geothermal reservoir, cold water flows faster in the fracture network, which may build up a sharp temperature gradient between fracture and matrix cells. Here we investigate how heat conduction of the rock can impact the thermal transport in a realistic fractured reservoir. Three values are selected to test the influence of heat conduction to thermal propagation in the formation and temperature profile at the production well.

The simulation results for different heat conduction are shown in Figure 14(a). When rock heat conduction is low, the production well indicates a very early thermal breakthrough. This can be explained by the fast flow in the fracture network, which carries the cold water forward to the production well. In comparison, the temperature drop is postponed in a larger heat conduction case, which is because cold water in the fracture is heated up to a larger extent with higher rock heat conduction.

Figure 15 shows the comparison of thermal distribution with different heat conductivity, which clearly displays the influence of heat conduction to thermal propagation in the reservoir. With the same volume of cold water injected, faster propagation of the temperature front is observed along the fracture network with small heat conduction.

For high-enthalpy systems, the heat conduction can also influence the phase transition process as shown in Figure 15. Due to the lower permeability of the matrix, only limited convective flow happens in the matrix so that heat conduction plays an important role in heat exchange between fracture and matrix. With larger heat conductivity, there is more heat exchanged through conduction so that more energy is extracted from the matrix and larger water saturation can be observed in the matrix cells near the production well.

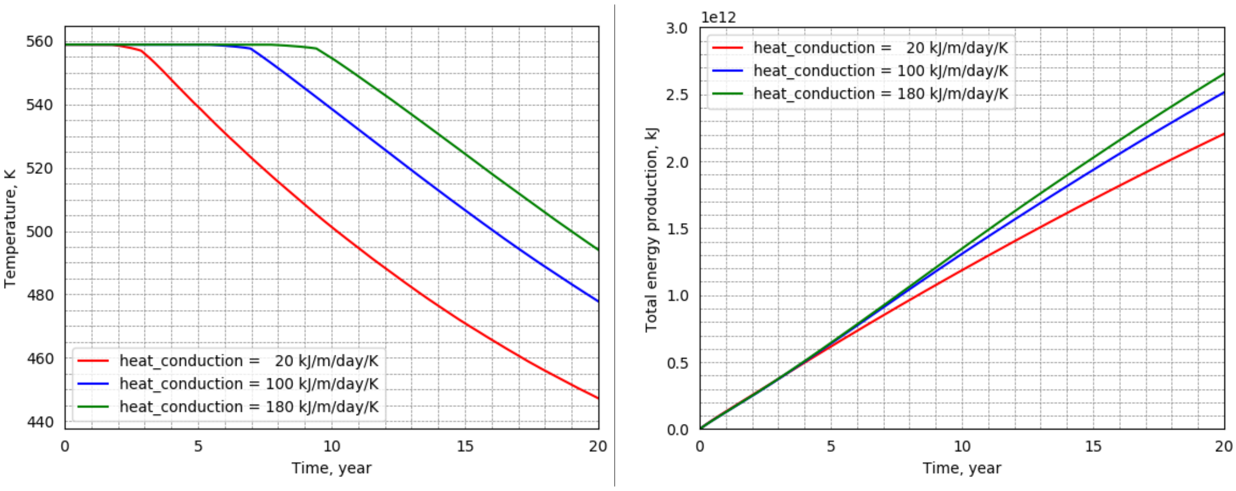

(a) **(b)**

Figure 14: Temperature and total energy production profile with different rock heat conduction.

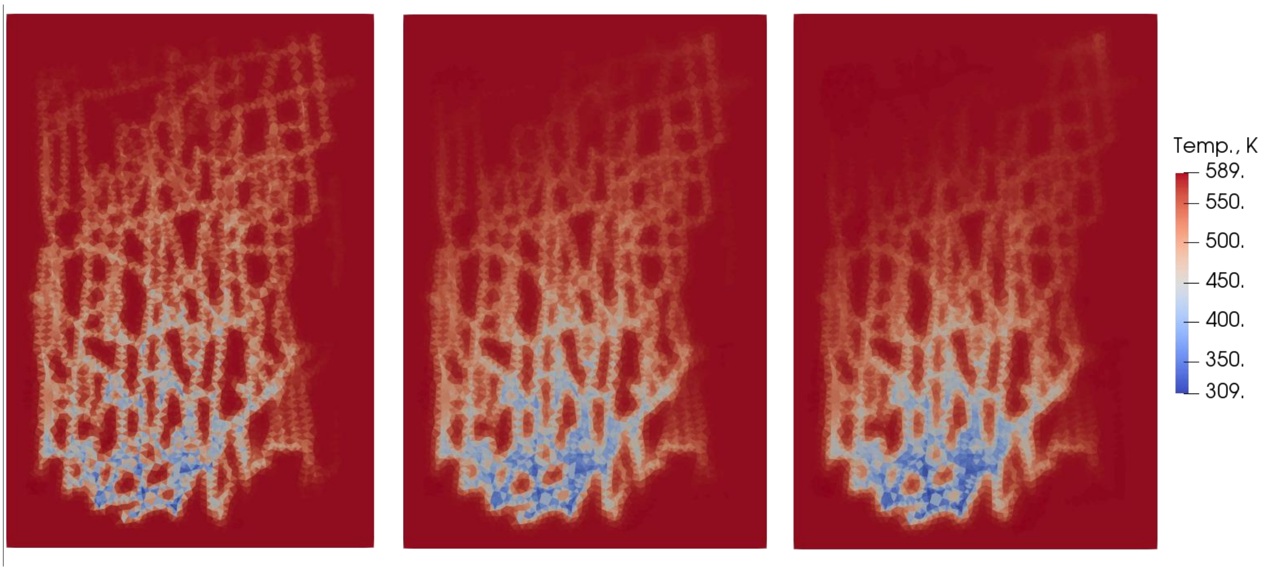

(a) **(b)** **(c)**

Figure 15: Temperature distribution with different rock heat conductivity (kJ/m/day/K) (a) 20 (b) 100 (c) 180.

4.3 Rock Heat Capacity

Rock heat capacity is relevant to the total energy contained in the reservoir rock. Here, three realistic values of rock heat capacity are chosen to investigate its influence to heat production.

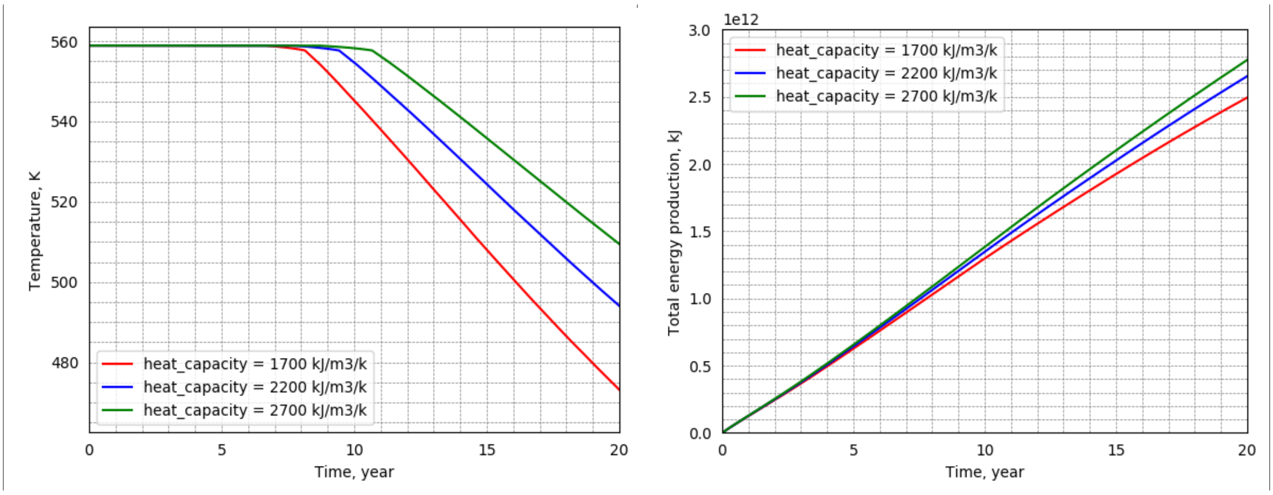

(a) **(b)**

Figure 16: Temperature and total energy production of production well with different heat capacity.

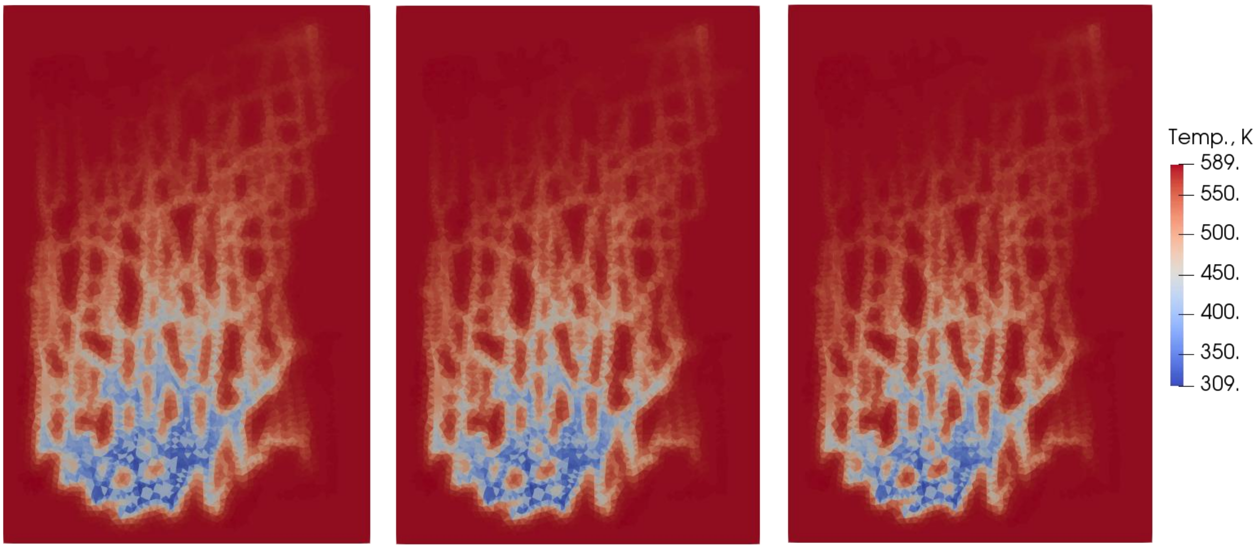

(a) **(b)** **(c)**

Figure 17: Temperature distribution with different heat capacity (kJ/m^3/K) (a) 1700 (b) 2200 (c) 2700.

As shown in Figure 16(a), the temperature drop at the production well is delayed with the increase of rock heat capacity, which is because the fluid obtains stronger heat recharge with higher heat capacity. Also, a larger amount of total energy is observed for higher heat capacity on the energy production curve. Figure 17 shows the influence of heat capacity to temperature propagation in a more straightforward way. For lower heat capacity, the cold front propagates faster and a wider cold front distribution is observed.

Due to the variation in heat capacity, the phase transition process varies correspondingly, which further influences the pressure distribution within the reservoir. We can see from Figure 18, the steam and water production rates increase with the increase in heat capacity, which means a larger pressure gradient is built up in the formation for a larger heat capacity scenario.

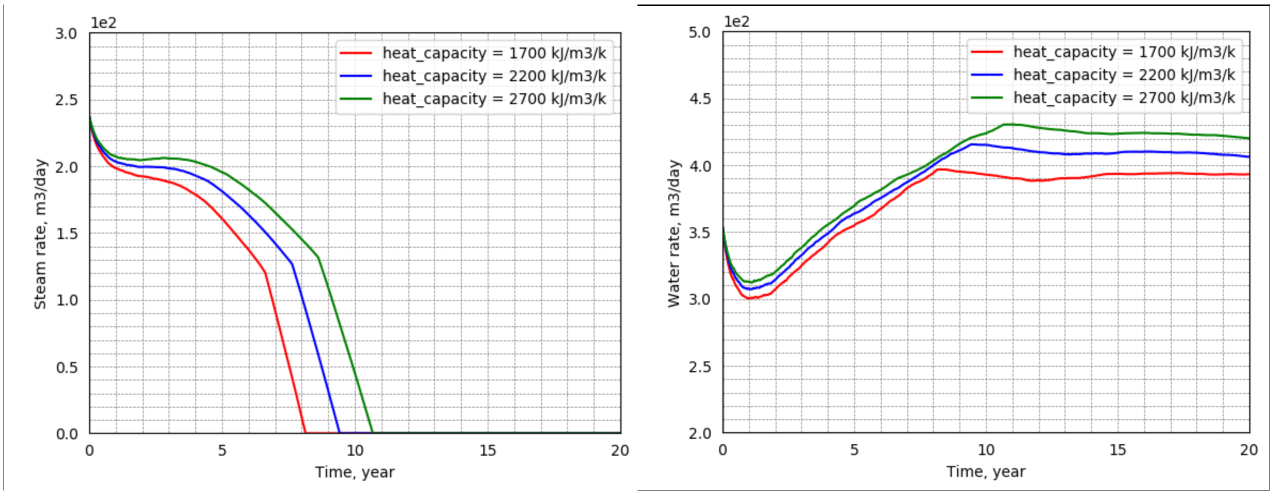

(a) **(b)**

Figure 18: Steam and water rate of production well with different heat capacity.

5. CONCLUSION

In this paper, a series of numerical simulations of a fractured high-enthalpy geothermal reservoir are performed using the Delft Advanced Research Terra Simulator. The realistic fractured geothermal reservoir is described with a discrete fracture-matrix model. Through convergence analysis of numerical results, an optimal set of grid discretization is selected with both accuracy and efficiency. Following this, a set of numerical experiments on different parameter settings is conducted. Systematical comparison of results shows that heat production and thermal propagation in fractured high-enthalpy geothermal reservoirs vary a lot with the uncertainties (i.e. fracture-matrix permeability ratio, rock heat conduction and heat capacity) in the formation.

For larger fracture-matrix permeability ratios, the fluid will primarily be transported in the fracture network and conductive flow dominates the thermal propagation. Therefore, faster thermal breakthrough is observed in the production well. For smaller permeability ratios, due to more uniform displacement in the reservoir, both conductive and convective flow can play an important role in thermal propagation, which is reflected on the temperature distribution map. With the increase of rock heat conduction and heat capacity, positive thermal response is observed on both the temperature profile and temperature distribution map. In comparison with rock heat capacity, rock heat conduction has a more nonlinear influence on the temperature profile and on the energy production curve.

The complex phase transition process in high-enthalpy geothermal systems distinguishes their development from their low-enthalpy counterparts. Simulations for high-enthalpy conditions facilitate a better understanding of the under-lying mechanisms (i.e., the interplay of conductive and convective heat flow in the presence of phase transition), and more accurately predict the heat and flow response to reservoir operations. Since there are not many publications on the effect of two-phase thermal transport in fractured high-enthalpy geothermal systems, this paper fills a gap in the literature and highlights the basic factors to be investigated for the development of such a resource.

REFERENCE

Berkowitz, B., 2002: Characterizing flow and transport in fractured geological media: A review. *Advances in Water Resources*, 25, 861-884.

Boersma, Q., Hardebol, N., Houben, M., Barnhoorn, A., & Drury, M., 2015: Fracture-fault network characterization of pavement imagery of the Whitby Mudstone, Yorkshire. EGU General Assembly Conference.

Coats, K. H., George, W. D., Chu C., and Marcum B. E., 1974: Three-dimensional simulation of steamflooding. *SPE Journal*, 14, 573-592.

Coats, K. H., 1980: Reservoir simulation: a general model formulation and associated physical/numerical sources of instability. *Boundary and Interior Layers-Computational and Asymptotic Methods*.

Collins, D.A., Nghiem, L.X., Li, Y.K. and Grabonstotter, J.E., 1992: An efficient approach to adaptive-implicit compositional simulation with an equation of state. *SPE Reservoir Engineering*, 7, 259-264.

DARTS, 2019: Delft Advanced Research Terra Simulator. *https://darts.citg.tudelft.nl*.

Gerke, H. H., van Genuchten, M. T., 1993a: A dual-porosity model for simulating the preferential movement of water and solutes in structured porous media. *Water Resources Research*, 29, 305-319.

Gerke, H. H., van Genuchten, M. T., 1993b: Evaluation of a first-order water transfer term for variably saturated dual-porosity flow models. *Water Resources Research*, 29, 1225-1238.

Jiang, J. and Younis, R.M., 2015: A multimechanistic multicontinuum model for simulating shale gas reservoir with complex fractured system. *Fuel*, 161, 333-344.

Karimi-Fard, M., Durlofsky, L. J., Aziz, K., 2004: An efficient discrete fracture model applicable for general-purpose reservoir simulators. *SPE Journal*, 9, 227- 236.

Karimi-Fard, M. and Durlofsky, L.J., 2016: A general gridding, discretization, and coarsening methodology for modeling flow in porous formations with discrete geological features. *Advances in Water Resources*, 96, 354-372.

Khait, M. and Voskov, D., 2018: Operator-based linearization for efficient modeling of geothermal processes, *Geothermics*, 74, 7-18.

Khait, M., Voskov, D., 2019: Integrated framework for modelling of thermal-compositional multiphase flow in porous media, *SPE Reservoir Simulation Conference*.

Lee, S. H., Jensen, C. L., Lough, M. F., 2000: Efficient finite-difference model for flow in a reservoir with multiple length-scale fractures. *SPE Journal*, 5(3), 268-275.

Li, L., Voskov, D., 2018: Multi-Level Discrete Fracture Model for Carbonate Reservoirs, *European Conference on the Mathematics of Oil Recovery*.

Pruess, K., Calore, C., Celati, R. and Wu, Y.S., 1987: An analytical solution for heat transfer at a boiling front moving through a porous medium. *International Journal of Heat and Mass Transfer*, 30, 2595-2602.

Shetty, S., Voskov, D. and Bruhn, D., 2018: Numerical Strategy for Uncertainty Quantification in Low Enthalpy Geothermal Projects, *43rd Workshop on Geothermal Reservoir Engineering, Stanford*.

The Geysers, 2019*:* *http://geysers.com/*.

Voskov, D.V. and Tchelepi, H.A., 2012: Comparison of nonlinear formulations for two-phase multi-component EoS based simulation, *Journal of Petroleum Science and Engineering*, 82, 101-111.

Voskov, D., 2017: Operator-based linearization approach for modeling of multiphase multi-component flow in porous media, *Journal of Computational Physics*, 337, 275-288.

Warren, J. E., Root, P. J., 1963: The behavior of naturally fractured reservoirs. *SPE Journal*, 3, 245-255.

Wang, Y., Khait, M., Voskov, D., Saeid, S. and Bruhn, D., 2019: Benchmark test and sensitivity analysis for Geothermal Applications in the Netherlands. *44th Workshop on Geothermal Reservoir Engineering, Stanford*.

Wang, Y. and Voskov, D., 2019: High-enthalpy geothermal simulation with continuous localization in physics. *44th Workshop on Geothermal Reservoir Engineering, Stanford*.

Wong, Z.Y., Horne, R., and Tchelepi, H., 2018: Sequential implicit nonlinear solver for geothermal simulation. *Journal of Computational Physics*, 368, 236-253.